analytical chemistry

pubs.acs.org/ac Article

Electrochemiluminescence Resonance Energy Transfer Biosensor Based on Self-Enhanced Terbium-Based Metal–Organic Frameworks with Antenna Effect for Sensitive MicroRNA-155 Detection

Ruiyan Liu, Zhuoxin Ye, Yongli Wu, Yan Zhang, Mo Ma, Pinyi Ma,* and Daqian Song*

Cite This: *Anal. Chem.* 2025, 97, 24706–24714 Read Online

ACCESS | Metrics & More | Article Recommendations | Supporting Information

ABSTRACT: The efficiency of electrochemiluminescence (ECL) emission relies heavily on the spatial proximity between luminophores and coreactant promoters. In conventional ternary systems, the diffusion-driven separation of components in solution often leads to energy loss and lower ECL efficiency. In this work, a self-enhanced lanthanide metal–organic framework (Ln-MOF) emitter, CuTb-BTC@AgNPs (CTBA), was constructed using Tb^{3+} as the luminophore, Cu^{2+} as the coreactant promoter, and Ag nanoparticles (AgNPs) as the electrical conductivity enhancer. An appropriate colocalization of these components significantly shortened the electron transfer distance between the luminescent group and the coreactant promoter, thereby enhancing the ECL efficiency. To modulate the signal, a $Pd@Cu_2O$ quencher, which has a broad UV–Vis absorption range, was introduced for resonance energy transfer (RET)-based suppression. A dual-output toehold-mediated strand displacement (TMSD) strategy was employed to enable target recycling and "on–off" signal control. Using microRNA-155 (miR-155), a biomarker implicated in multiple cancers, as a model target, the biosensor exhibited a wide linear detection range from 10 aM to 1 nM and an ultralow detection limit of 4.7 aM. It also had excellent specificity and achieved high recovery rates when applied to detect human serum and cancer cell samples. Overall, this work describes a robust strategy for integrating Ln-MOF emission platforms with nucleic acid amplification, presenting a powerful tool for the ultrasensitive detection of clinically relevant miRNA.

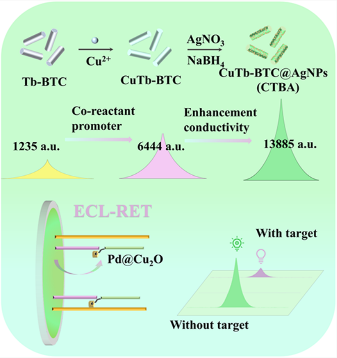

■ INTRODUCTION

Electrochemiluminescence (ECL) is a powerful analytical technique due to its high sensitivity, wide dynamic range, and negligible background signal.[1] These advantages have led to its broad application in clinical diagnostics,[2] environmental monitoring,[3] and food safety.[4] Central to the performance of ECL-based biosensors is the development of highly efficient and stable luminophores. Traditional luminophores, such as $[Ru(bpy)_3]^{2+}$ and luminol, have long served as foundational components in ECL systems.[5,6] However, their small molecular size and high susceptibility to leakage often lead to poor signal stability and low reproducibility. In recent years, metal–organic frameworks (MOFs) have attracted considerable attention as ECL-active materials due to their high porosity, tunable structures, and chemical stability.[7,8] MOFs can be used as hosts for encapsulating[9] or incorporating luminophores[10] to improve their structural integrity and photostability. Among various MOF-based luminophores, lanthanide-based MOFs (Ln-MOFs) are notable for their unique photophysical properties, including long luminescence lifetimes, sharp emission bands, and large Stokes shifts.[11] These properties make Ln-MOFs particularly attractive for use in ECL systems. Furthermore, the antenna effect, in which organic ligands absorb excitation energy and transfer it to the lanthanide center, can significantly enhance emission efficiency.[12] Although Eu-based MOFs have been largely studied,[13] terbium (Tb)-based MOFs remain underexplored despite their excellent green luminescence and favorable quantum efficiency. Therefore, developing self-luminescent Tb-MOFs as ECL emitters represents a promising but underutilized strategy.

MicroRNAs (miRNAs) are small, noncoding RNAs that regulate gene expression post-transcription.[14] They play critical roles in various biological processes including cell proliferation, differentiation, and apoptosis. Aberrant expression of specific miRNAs has been found to be closely associated with the onset and progression of multiple cancers, making them important diagnostic and prognostic biomarkers.[15] For instance, microRNA-155 (miR-155) is overexpressed in lung,[16] breast,[17] and pancreatic malignancies.[18] However, the low abundance and sequence similarity of miRNA family members along with their high susceptibility to degradation make the accurate and sensitive detection of these molecules significantly challenging.

Received: August 13, 2025
Revised: October 23, 2025
Accepted: October 24, 2025
Published: October 29, 2025

ACS Publications

https://doi.org/10.1021/acs.analchem.5c04977

Scheme 1. Schematic Diagram of an "On−Off" ECL-Based miR-155 Detection Platform[a]

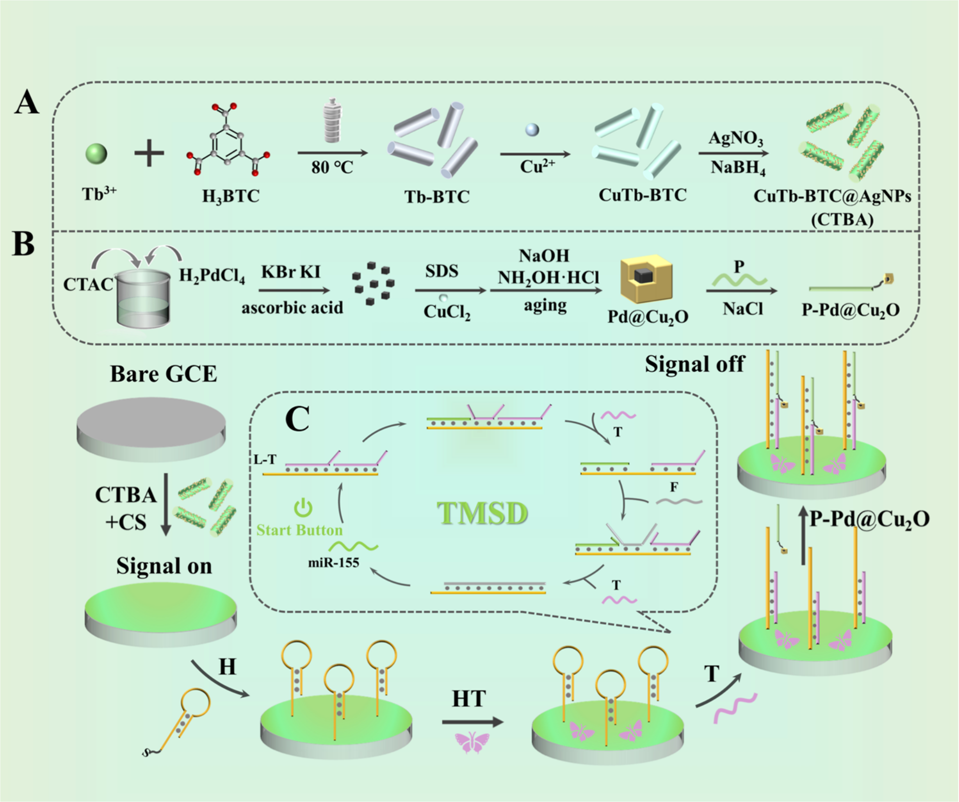

[a](A) Synthesis of CTBA. (B) Synthesis of $P-Pd@Cu_2O$. (C) TMSD amplification process.

Consequently, developing rapid, ultrasensitive, and selective biosensing strategies for miRNA detection is important for advancing precision medicine.

ECL sensing is particularly well-suited for miRNA detection due to its high signal-to-noise ratio (S/N) and compatibility with nanomaterial-assisted signal amplification.[19,20] In attempts to improve ECL efficiency, coreactant promoters have been employed to catalyze the decomposition of oxidants (such as $K_2S_2O_8$) and generate highly reactive intermediates (such as $SO_4^{\bullet-}$ radicals) that drive the ECL process. Since Ma et al. first introduced aminourea as a coreactant promoter in the $S_2O_8^{2-}$ cathodic ECL system,[21] a variety of similar nanomaterials have been developed. Representative examples include metal nanoclusters (e.g., gold and silver clusters),[22] metal oxides (e.g., TiO_2 and $Fe_3O_4-CeO_2$),[23] and organic or hybrid structures (Ru@MOF, IRMOF-3, and Ag^+@UiO-66-NH_2).[24] These materials can efficiently enhance the decomposition of $K_2S_2O_8$ and amplify the ECL signal. However, in most of these systems, the coreactant promoter and the luminophore are not colocalized within a single nanostructure. This spatial separation often leads to inefficient electron transfer and signal loss. To overcome this limitation, researchers have proposed integrated systems that embed both functionalities to improve the ECL signal output. For example, Zn-TCPP has been coupled with a Co−N copromoter via ligand exchange, therefore achieved improved ECL output.[25]

Inspired by these insights, herein, we report a self-enhanced ECL emitter consisting of Tb^{3+} as the luminophore, Cu^{2+} as the coreactant promoter, and Ag nanoparticles (AgNPs) as the electrical conductivity enhancer. The emitter was denoted as CuTb-BTC@AgNPs (CTBA). As shown in Scheme 1A, Tb-BTC was synthesized by using H_3BTC as an antenna ligand, and Cu^{2+} was incorporated into it through ion-exchange mechanisms to accelerate the generation of $SO_4^{\bullet-}$ from $K_2S_2O_8$. AgNPs were then deposited via postsynthetic modification (PSM) to facilitate charge transfer and further enhance ECL emission. To construct an ECL resonance energy transfer (ECL-RET) system, a core−shell $Pd@Cu_2O$ nanostructure, which has a broad UV−Vis absorption range, was synthesized and functionalized with P DNA strands. This nanostructure acts as a quencher (Scheme 1B). Moreover, a dual-output toehold-mediated strand displacement (TMSD) amplification strategy was introduced to allow for signal regulation and target recycling (Scheme 1C). Specifically, miR-155 initiated strand displacement reactions, leading to the release of T strands and the recycling of miR-155, thereby allowing sensitive "on−off" signal modulation on the electrode. This work presents a rationally engineered, multifunctional biosensing platform that combines Ln-MOF luminophores, a coreactant promoter, ECL-RET quenching, and nucleic acid amplification. The proposed strategy can be employed to enhance the ECL performance for the sensitive and selective detection of miR-155, a key biomarker implicated in various cancers.

■ EXPERIMENTAL SECTION

Synthesis of Tb-BTC. Tb-BTC was synthesized via a reported hydrothermal method with slight modifications.[26] Briefly, 0.56 mmol of $Tb(NO_3)_3·6H_2O$ (254 mg), 0.2 mmol of H_3BTC (42 mg), and 0.8 mmol of CH_3COONa (66 mg) were dissolved in a solution containing 16 mL of DMF and 8 mL of deionized water at room temperature. The mixture was

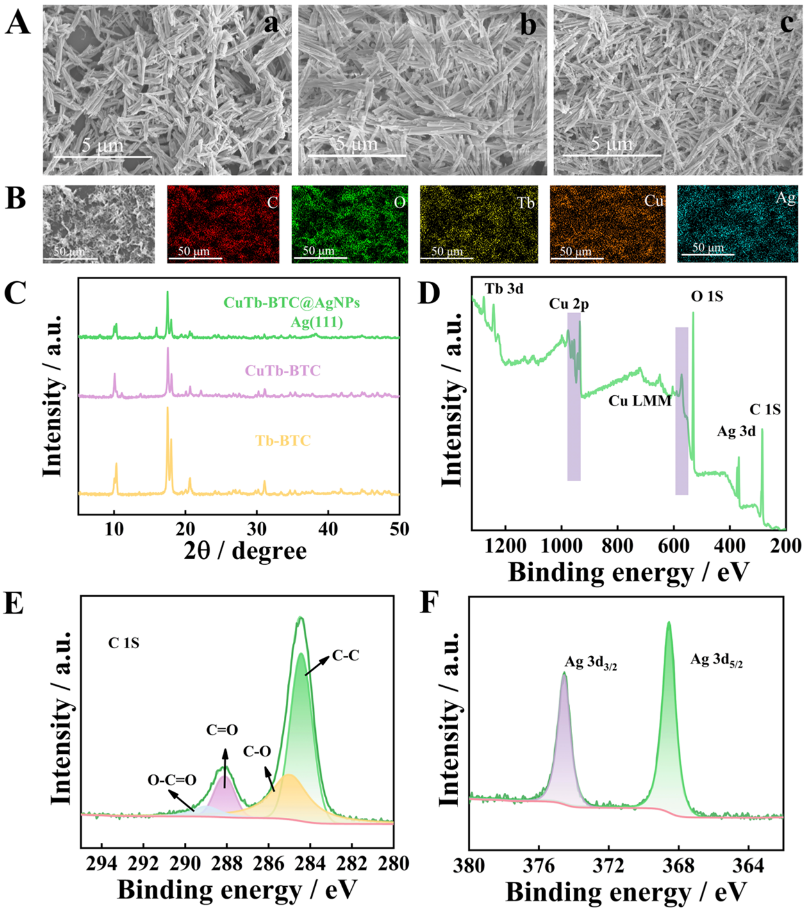

Figure 1. Characterization of CTBA. (A) SEM images of Tb-BTC, CuTb-BTC, and CTBA (scale bar: 5 μm). (B) EDS mapping of CTBA, showing the distribution of C, O, Tb, Cu, and Ag (scale bar: 50 μm). (C) XRD spectra of Tb-BTC, CuTb-BTC, and CTBA. (D) XPS spectrum of CTBA. (E) XPS spectrum of C 1s. (F) XPS spectrum of Ag $3d_{3/2}$ and Ag $3d_{5/2}$.

transferred to a Teflon-lined autoclave and heated at 80 °C for 24 h. After being cooled to room temperature, the product was washed three times with ethanol and collected by centrifugation at 8000 rpm for 10 min. The solid was then dried in a vacuum oven at 60 °C for 8 h.

Synthesis of CuTb-BTC. CuTb-BTC was prepared via an ion-exchange method.[27] Specifically, 60.4 mg of $Cu(NO_3)_2$ was dissolved in 5 mL of water, and the mixture was sonicated for 3 min. After 10 mg of Tb-BTC was added, the mixture was stirred at 60 °C for 4 h. The product was collected by centrifugation (8000 rpm, 10 min), washed with ultrapure water, and vacuum-dried at 60 °C for 4 h.

Synthesis of CTBA. CTBA was prepared via a PSM approach.[28] First, 10 mg of CuTb-BTC was dispersed in 5 mL of ultrapure water and then ultrasonicated. After 100 μL of 0.1 M $AgNO_3$ was added, the mixture was stirred for 2 h, and 100 μL of 0.3 M $NaBH_4$ was added thereafter. The reaction mixture was stirred for another 30 min. The resulting product was washed twice with ultrapure water, collected by centrifugation (8000 rpm, 10 min), redispersed in 5 mL of water, and then stored at 4 °C.

Synthesis of Pd Nanoparticles (PdNPs). PdNPs were synthesized following a previously reported method.[29] In a water bath at 35 °C, 48 mg of cetyltrimethylammonium chloride, 9.125 mL of deionized water, and 0.7 mL of 10 mM H_2PdCl_4 (prepared by dissolving 17.8 mg of $PdCl_2$ in 10 mL of 20 mM HCl) were mixed thoroughly. While the mixture was continuously stirred, 500 μL of 1 mM KBr and 50 μL of 1 mM KI were added. After 10 min, 1.2 mL of 50 mM ascorbic acid was added, and the reaction was allowed to proceed for 30 min. The obtained product was washed twice with ultrapure water and centrifuged at 7500 rpm for 10 min. The final PdNPs were dispersed in 400 μL of deionized water.

Synthesis of Pd@Cu_2O. First, 87 mg of sodium dodecyl sulfate was dissolved in 5 mL of deionized water. Then, 100 μL of 0.1 M $CuCl_2$ and 100 μL of PdNPs solution were added sequentially. Following the addition of 250 μL of 1 M NaOH, the mixture was shaken for 10 s, after which 150 μL of 0.2 M $NH_2OH{\cdot}HCl$ was added. The mixture was incubated at room temperature for 2 h. The resulting Pd@Cu_2O particles were washed three times with a 1:1 (v/v) water−ethanol solution and centrifuged at 5000 rpm for 5 min.

Synthesis of P−Pd@Cu_2O. P−Pd@Cu_2O conjugates were synthesized via thiol-metal self-assembly.[30] Briefly, Pd@Cu_2O was suspended in 2 mL of PBS (0.01 M, 0.1% Tween-20, pH 7.0) and sonicated for 30 min. Thiolated DNA probe P (5 μM) was pretreated with 2.5 μL of 0.5 M TCEP for 30 min to reduce the disulfide bonds. The activated DNA was then added to the Pd@Cu_2O suspension, and the mixture was shaken at room temperature for 12 h. After NaCl was added to a final concentration of 0.1 M, the mixture was shaken for another 24 h. Excess DNA was removed by centrifugation and washing. The final product was resuspended in 150 μL of a Tris−HCl buffer and stored for further use.

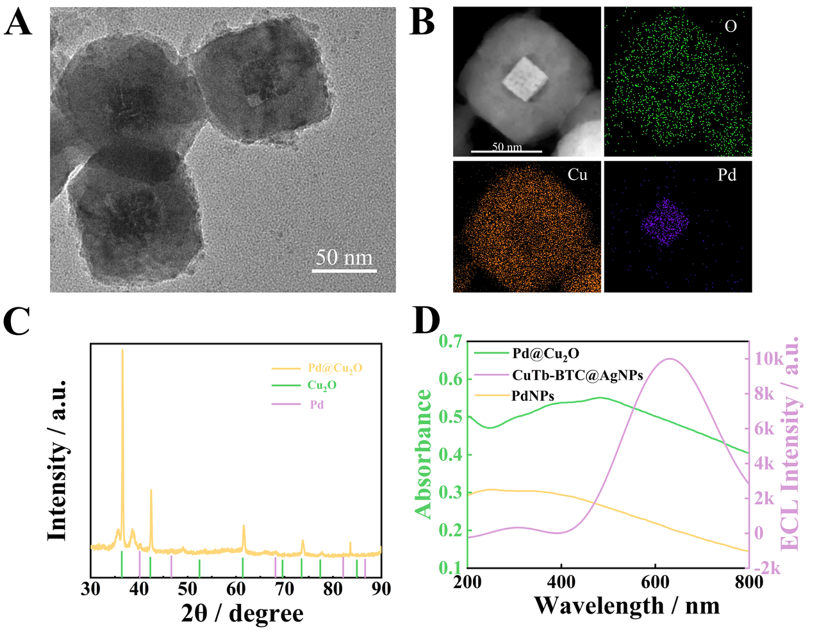

Figure 2. Characterization of Pd@Cu$_2$O. (A) TEM images of Pd@Cu$_2$O (scale bar = 50 nm). (B) EDS mapping of Pd@Cu$_2$O showing the distribution of Pd, O, and Pd(I) (scale bar = 50 nm). (C) XRD spectra of Pd, Cu$_2$O, and Pd@Cu$_2$O. (D) Spectral overlap between the ECL emission of CTBA (purple curve) and UV−Vis absorption spectra (orange curve) of the Pd cores and Pd@Cu$_2$O (green curve).

Dual-Output TMSD Amplification Reaction. DNA strands L, T, and F were dissolved in Tris−HCl (pH 7.4). A three-stranded DNA complex was formed by mixing 5 μL of 30 μM L and 10 μL of 30 μM T, heating at 95 °C for 5 min, and then cooling to room temperature at a rate of 1 °C/min. For target recognition, miR-155 at varying concentrations was incubated with 3 μL of the prepared DNA complex and 1.5 μL of 20 μM F at 37 °C for 2 h.

ECL-Based Biosensor Fabrication and ECL Measurement. A bare glassy carbon electrode (GCE) was polished with 0.3 and 0.05 μm alumina powder and then cleaned via ultrasonication in ethanol and ultrapure water. Subsequently, 10 μL of a solution containing CTBA (2 mg/mL) and chitosan (CS, 0.5%) was deposited onto the GCE surface and then oven-dried at 37 °C to obtain CTBA(CS)/GCE. Then, 10 μL of 2 μM H (treated with TCEP) was applied on CTBA(CS)/GCE and incubated overnight at room temperature to obtain H/CTBA(CS)/GCE. After that, 10 μL of 1 μM HT was dropped onto H/CTBA(CS)/GCE and incubated in an oven at 37 °C for 30 min to obtain HT/H/CTBA(CS)/GCE. To prepare T/HT/CTBA(CS)/GCE, 10 μL of the amplification reaction solution was applied on the surface of HT/H/CTBA(CS)/GCE and incubated at 37 °C for 2 h. Finally, to obtain P−Pd@Cu$_2$O/T/HT/H/CTBA(CS)/GCE, 10 μL of 5 μM P−Pd@Cu$_2$O was dropped onto the surface of T/HT/H/CTBA(CS)/GCE and incubated in an oven at 37 °C for 2 h. ECL measurements were conducted in 2 mL of 50 mM $K_2S_4O_8$ (pH 7.4) by using a three-electrode system. The potential was scanned from −1.7 to 0 V (vs Ag/AgCl) at a scan rate of 300 mV/s. The photomultiplier tube voltage was set to 800 V, and the amplification series was set at 4.

■ RESULTS AND DISCUSSION

Characterizations of CTBA. The morphologies of Tb-BTC, CuTb-BTC, and CTBA were examined by scanning electron microscopy (SEM). As shown in Figure 1A, all three materials had short-rod morphologies, indicating that the incorporation of Cu^{2+} and AgNPs had no impact on the original crystal shape of Tb-BTC. Additionally, AgNPs were observed on the surface of CuTb-BTC, confirming successful deposition. Elemental mapping using energy-dispersive spectroscopy (EDS) revealed a homogeneous distribution of C, O, Tb, Cu, and Ag in CTBA (Figure 1B), which is consistent with the expected composition. X-ray diffraction (XRD) analysis further confirmed the successful synthesis and structural integrity of the MOFs. As shown in Figure 1C, CTBA and CuTb-BTC exhibited the characteristic diffraction peaks of Tb-BTC.[31] Notably, a new diffraction peak appeared at 38.3° in CTBA. This peak corresponds to the (111) plane of metallic Ag, which is indicative of the successful loading of AgNPs. The elemental composition of CTBA was further analyzed by X-ray photoelectron spectroscopy (XPS). As shown in Figure 1D, the spectrum confirmed the presence of Tb 3d, Cu 2p, Cu LMM, O 1s, and C 1s. Peak deconvolution of the C 1s spectrum (Figure 1E) revealed the characteristic peaks corresponding to C−C, C═O, C−O, and O−C═O, confirming the presence of the organic linker H_3BTC. The Ag 3d spectrum (Figure 1F) exhibited peaks at 368.5 eV (Ag $3d_{5/2}$) and 374.5 eV (Ag $3d_{3/2}$), confirming the presence of AgNPs.[32] Additional XPS spectra of Tb and Cu are provided in Figure S1. Peaks at 934.9 and 954.9 eV (Cu $2p_{3/2}$ and Cu $2p_{1/2}$, respectively), along with a satellite peak at 943.1 eV and a Cu LMM peak at ∼572 eV, confirmed the oxidation state of Cu as Cu^{2+}.[33] Fourier-transform infrared (FTIR) spectroscopy was used to study the coordination environments of H_3BTC, Tb-BTC, and CuTb-BTC (Figure S2). In H_3BTC, characteristic bands at 1720 cm^{-1} (C═O stretching), 3088−2558 cm^{-1} (O−H stretching), and 916 cm^{-1} (O−H out-of-plane bending) were observed. In Tb-BTC, these bands disappeared and new peaks at 1615−1543 and 1433−1383 cm^{-1} (corresponding to the asymmetric and symmetric COO^- stretching vibrations, respectively) were observed, which is indicative of the successful coordination between carboxylate groups of H_3BTC and Tb^{3+}. In CuTb-BTC, the COO^- bands

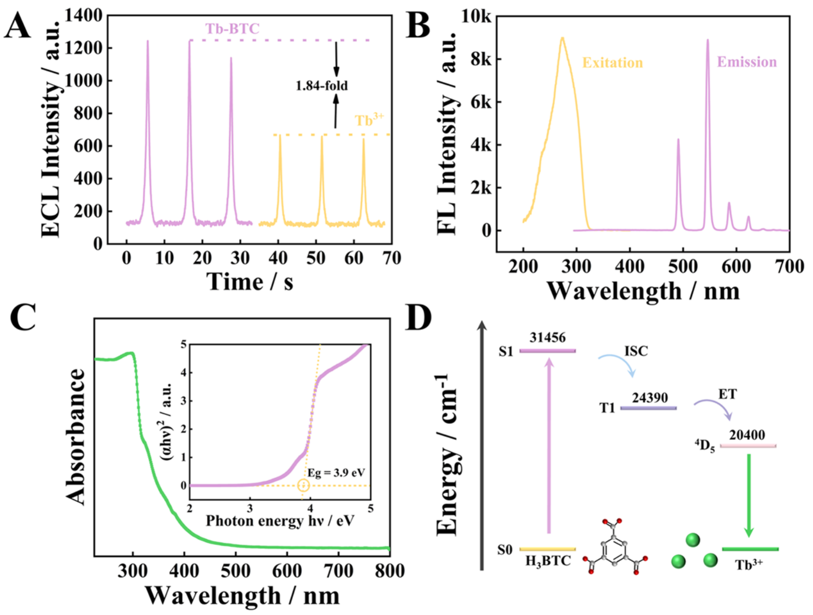

Figure 3. Experiments verifying the antenna effect of Tb-BTC. (A) Comparison of the ECL signals between Tb-BTC and Tb^{3+} in 10 mM PBS (pH 7.4) containing 50 mM $K_2S_2O_8$. (B) FL excitation and emission spectra of CTBA. (C) Solid-state UV−Vis spectra of H_3BTC. (D) Schematic diagram of the ET process from H_3BTC to Tb^{3+} in Tb-BTC.

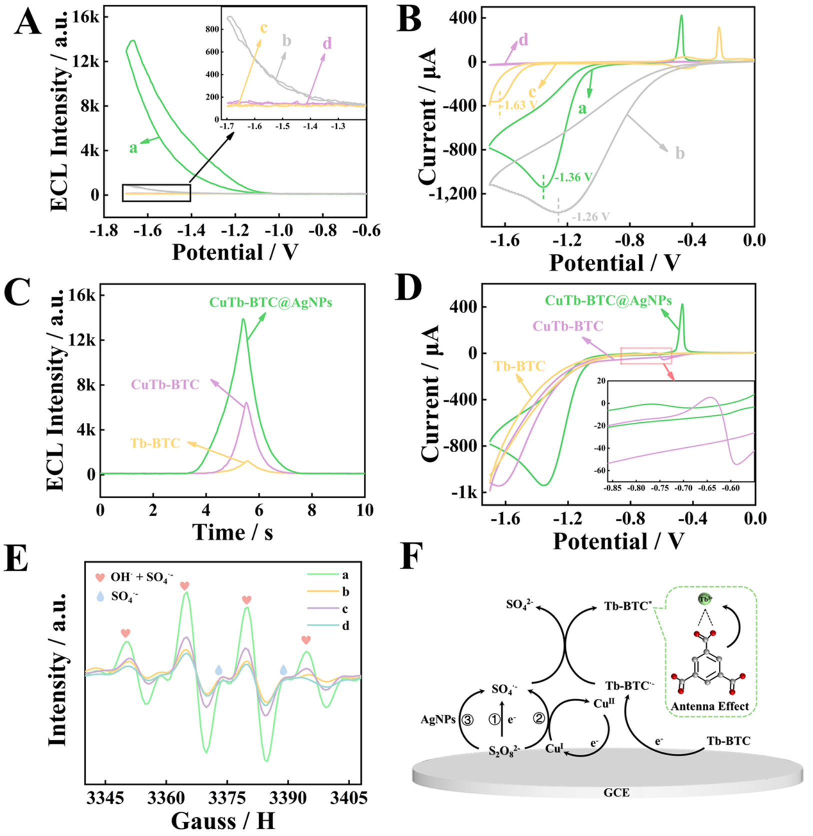

Figure 4. ECL and CV measurements illustrating the ECL mechanism. (A) ECL response and (B) CV of CTBA/GCE in 10 mM PBS (pH 7.4) containing 50 mM $K_2S_2O_8$ (curve a); bare GCE in 10 mM PBS (pH 7.4) containing 50 mM $K_2S_2O_8$ (curve b); CTBA/GCE in 10 mM PBS (pH 7.4) without $K_2S_2O_8$ (curve c); and bare GCE in 10 mM PBS (pH 7.4) without $K_2S_2O_8$ (curve d). (C) ECL response and (D) CV of Tb-BTC/GCE, CuTb-BTC/GCE, and CTBA/GCE in 10 mM PBS (pH 7.4) containing 50 mM $K_2S_2O_8$. (E) The in situ electrical EPR spectra in the presence of $K_2S_2O_8$ and DMPO with CTBA/GCE (curve a), CuTb-BTC/GCE (curve b and curve c), and Tb-BTC/GCE (curve d). (F) Schematic diagram of the proposed ECL mechanism of CTBA/GCE: ① $S_2O_8^{2-}$ acts as a coreactant; ② Cu^{2+} serves as a coreactant promoter; and ③ AgNPs further enhance the reduction process.

remained observable, suggesting that Cu^{2+} may replace part of Tb^{3+} through ion exchange without disrupting the MOF structure.[34] The ECL performance of CTBA was also evaluated. The results (Figure S3) demonstrated that CTBA had excellent stability and repeatability and high storage performance.

Characterizations of $Pd@Cu_2O$. The morphology of the quencher material, $Pd@Cu_2O$, was examined by using transmission electron microscopy (TEM). As shown in Figure 2A, the composite had a uniform cubic core−shell structure with an average diameter of ∼ 100 nm.[35] EDS elemental mapping (Figure 2B) indicated the presence of Pd, Cu, and O, confirming the successful formation of $Pd@Cu_2O$. XRD patterns of $Pd@Cu_2O$ (Figure 2C) exhibited distinct peaks at 40.05, 46.66, and 68.12°, corresponding to the (111), (200), and (220) planes of Pd (JCPDS No. 46-1043). Additional characteristic peaks of Cu_2O at 36.58, 42.49, 61.58, and 73.77°, corresponding to the (111), (200), (220), and (311) planes (JCPDS No. 34-1354), confirmed successful Cu_2O coating.[36] To evaluate the feasibility of RET between the emitter and quencher, the ECL emission spectrum of CTBA and the UV−Vis absorption spectrum of $Pd@Cu_2O$ were measured (Figure 2D). The measurement showed that CTBA exhibited a strong ECL emission peak at 627.3 nm, which overlapped with the broad UV−Vis absorption band of $Pd@Cu_2O$ in the 200−800 nm range. This spectral overlap suggests that photons emitted from CTBA can be efficiently absorbed by $Pd@Cu_2O$, indicating the potential occurrence of ECL-RET quenching.

Antenna Effect-Induced ECL Emission of Tb-BTC. To investigate the luminescence mechanism of Tb-BTC, its ECL intensity was compared to that of free Tb^{3+} under identical conditions. As shown in Figure 3A, the ECL signal of Tb-BTC was 1.84 times higher than that of Tb^{3+} alone, indicative of an improved emission efficiency. To explore the underlying mechanism, the fluorescence (FL) excitation and emission spectra of Tb-BTC were recorded (Figure 3B). The maximum excitation and emission wavelengths were observed at 274.8 and 546.3 nm, respectively, consistent with the typical emissions of Tb^{3+}.[37] The similarity between FL and ECL emission profiles suggests that both proceeded through analogous processes involving ground-state excitation, excited-state relaxation, and luminescence. This enhancement is likely attributed to the antenna effect, wherein the H_3BTC ligand serves as a sensitizer by transferring energy to the Tb^{3+} center, thereby amplifying the luminescence. To verify the efficiency of energy transfer, the energy levels involved in the sensitization process were analyzed using Reinhoudt's criterion.[38] According to this model, effective ligand-to-metal energy transfer requires (1) a sufficiently large singlet−triplet energy gap ($\triangle E_{S1\text{-}T1} = E_{S1} - E_{T1} > 5000\ cm^{-1}$) to enable intersystem crossing (ISC); and (2) a suitable triplet−acceptor gap ($\Delta E_{T1\text{-}Tb} = E_{T1} - E_{Tb} > 3500\ cm^{-1}$) to ensure efficient energy transfer. Based on the absorption edge in the solid-state UV−Vis spectrum of H_3BTC (Figure 3C), the singlet energy level (S_1) was estimated to be 31456 cm^{-1}.[39] According to the literature, the triplet state energy (T_1) of H_3BTC is approximately 24390 cm^{-1},[40] and the excited-state energy of Tb^{3+} is about 20400 cm^{-1}.[41,42] These values yield energy gaps of $\triangle E_{S1\text{-}T1} = 7066\ cm^{-1}$ and $\Delta E_{T1\text{-}Tb} = 3990\ cm^{-1}$, both exceeding the required thresholds (Figure 3D). These results confirm that H_3BTC effectively absorbed excitation energy, underwent ISC to the T_1 state, and transferred energy to Tb^{3+} via the antenna effect, thereby enhancing the ECL signal.

ECL Mechanism of CTBA. The ECL behavior of CTBA in the presence of $S_2O_8^{2-}$ was systematically investigated by using ECL and cyclic voltammetry (CV). As shown in Figure 4A,B, no significant ECL signal or reduction peak was observed on a bare GCE in the absence of the coreactant (curve d). Upon the addition of $S_2O_8^{2-}$, a weak ECL signal (915 au) and a reduction peak at −1.26 V appeared (curve b). This indicates that the electrochemical reduction of the coreactant occurred on the electrode. In PBS, the ECL signal of CTBA/GCE was negligible. An oxidation peak was observed at −1.63 V (curve c). This peak corresponds to the reduction peak of CTBA on the GCE. The results presented above indicate that the reduction of $S_2O_8^{2-}$ on the bare electrode occurred prior to the reduction of CTBA on the electrode. In the $S_2O_8^{2-}$/PBS system, CTBA/GCE exhibited a reduction peak at −1.36 V and a strong ECL signal of 13,885 au (curve a). The shift in the reduction peak and the enhanced ECL emission were attributed to the promoting effects of $S_2O_8^{2-}$ in combination with the coreactant promotors, Cu^{2+} and AgNPs.

To further clarify the role of each component in CTBA, the ECL performances of Tb-BTC, CuTb-BTC, and CTBA were compared (Figure 4C). Upon the introduction of Cu^{2+}, the reduction peak shifted from −1.65 to − 1.62 V, and additional redox peaks corresponding to the Cu^{2+}/Cu^{+} redox couple appeared at −0.65 and − 0.58 V.[43] After AgNPs loading, a new reduction peak appeared near −0.45 V,[44] and the overall reduction potential shifted positively to −1.36 V. These results indicate that both Cu^{2+} and AgNPs accelerated the reduction of $S_2O_8^{2-}$ and contributed to the generation of $SO_4^{\bullet-}$, thereby enhancing ECL kinetics (Figure 4D). Using 5,5-dimethyl-1-pyrroline *N*-oxide (DMPO) as a spin-trapping agent, free radicals present in a PBS solution containing $K_2S_2O_8$ were detected. As shown in Figure 4E, when Tb-BTC, CuTb-BTC, and CTBA were modified on the electrode surface, the peak intensities of DMPO−$OH^{\bullet}$ and DMPO−$SO_4^{\bullet-}$ in the electron paramagnetic resonance (EPR) spectra gradually increased, indicating the high catalytic efficacy of Cu^{2+} and AgNPs (curves d, c, a). Furthermore, we tested the EPR spectra of CuTb-BTC with different Cu^{2+} contents. Curves b and c reveal that CuTb-BTC with a higher Cu^{2+} content produced more $SO_4^{\bullet-}$, further confirming that Cu^{2+} promotes the generation of $SO_4^{\bullet-}$. The proposed ECL mechanism involves three synergistic processes (Figure 4F):

(1) Coreactant reduction pathway:

$$S_2O_8^{2-} + e^- \rightarrow SO_4^{\bullet-} + SO_4^{2-} \tag{1}$$

$$\text{Tb-BTC} + e^- \rightarrow \text{Tb-BTC}^{\bullet-} \tag{2}$$

$$\text{Tb-BTC}^{\bullet-} + SO_4^{\bullet-} \rightarrow \text{Tb-BTC}^{*} + SO_4^{2-} \tag{3}$$

(2) Cu^{2+}-assisted redox cycling:

$$Cu^{II} + e^- \rightarrow Cu^{I} \tag{4}$$

$$Cu^{I} + S_2O_8^{2-} \rightarrow Cu^{II} + SO_4^{2-} + SO_4^{\bullet-} \tag{5}$$

(3) AgNP catalytic cycle and reactive oxygen species generation:

$$Ag^0 + Ag^+ \rightarrow Ag^0 - Ag^+ \tag{6}$$

$$2Ag^0 - Ag^+ \rightarrow Ag^{2+} - Ag^{2+} \tag{7}$$

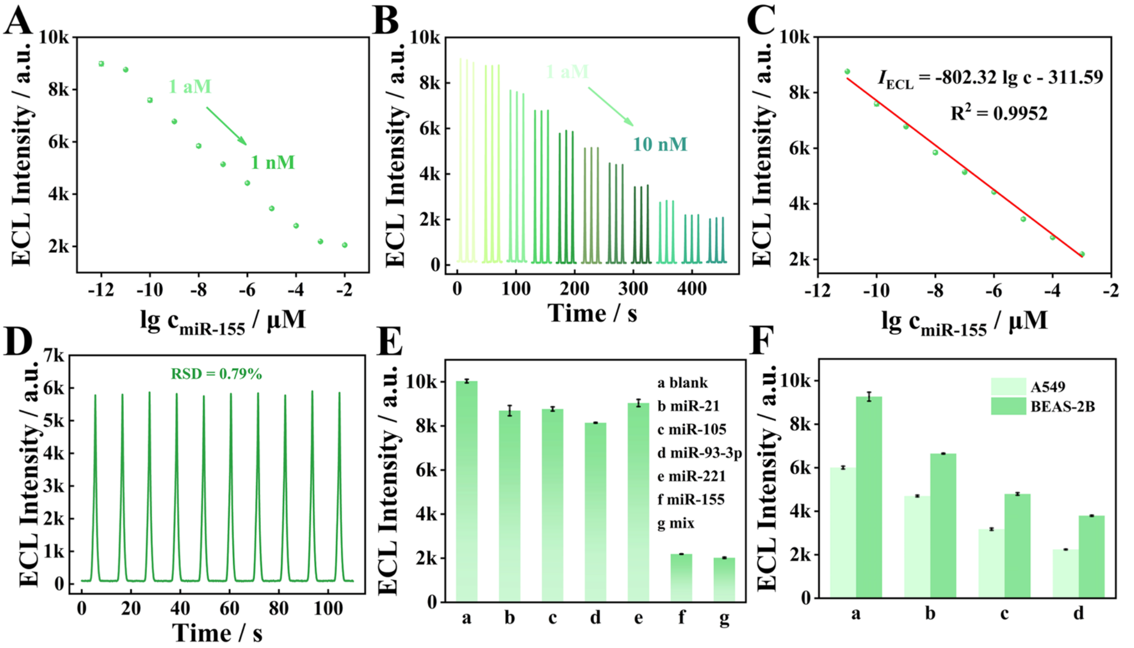

Figure 5. Analytical performance of the prepared ECL biosensor in miR-155 detection. (A) Response of the ECL biosensor to miR-155 at different concentrations (1 aM, 10 aM, 100 aM, 1 fM, 10 fM, 100 fM, 1 pM, 10 pM, 100 pM, 1 nM, and 10 nM). (B) Stability of the ECL biosensor in detecting miR-155 at different concentrations (1 aM, 10 aM, 100 aM, 1 fM, 10 fM, 100 fM, 1 pM, 10 pM, 100 pM, 1 nM, and 10 nM). (C) Calibration curve showing the relationship between ECL intensity and log (miR-155 concentration) (n = 3, from 10 aM to 1 nM). (D) Stability of ECL intensity during detection of 10 fM miR-155 for 10 successive 10 scans. (E) Selectivity of the biosensor to a blank sample, miR-155 (10 nM) alone, 100 nM interfering miRNAs (miR-21, miR-105, miR-93-3p, and miR-221), and mixtures of miR-155 (10 nM) and interfering miRNAs (100 nM) in 0.1 M PBS (pH 7.4) containing 50 mM $K_2S_2O_8$. Scanning range: −1.7 to 0 V. Scanning rate: 300 mV·s^{-1}. (F) ECL intensity of the biosensor during the detection of miR-155 in A549 and BEAS-2B cells at varying cell counts: (a) 1 × 10^2, (b) 1 × 10^3, (c) 1 × 10^4, and (d) 1 × 10^5 cells.

$$S_2O_8^{\ 2-} + (Ag^{2+} - Ag^{2+}) \rightarrow Ag^{2+} + SO_4^{\ 2-} + SO_4^{\ \bullet -} + Ag^{2+} + Ag^0 \quad (8)$$

$$2Ag^{2+} + H_2O \rightarrow Ag^+ + AgO^+ + 2H^+ \quad (9)$$

$$AgO^+ + H_2O \rightarrow Ag^+ + H_2O_2 \quad (10)$$

$$H_2O_2 + e^- \rightarrow OH^- + OH^\bullet \quad (11)$$

$$OH^\bullet + S_2O_8^{\ 2-} \rightarrow SO_4^{\ \bullet -} + HSO_4^{\ -} + O_2 \quad (12)$$

$$O_2 + H_2O + e^- \rightarrow OH^- + H_2O_2 \quad (13)$$

Through the synergistic action between Cu^{2+} and AgNPs, the generation of $SO_4^{\ \bullet -}$ and other reactive oxygen species was greatly accelerated. This acceleration facilitates the excitation of Tb-BTC, leading to a significantly enhanced ECL emission.

Performance of the Constructed ECL Sensor. Prior to performance evaluation, the feasibility of the dual-output TMSD amplification strategy was confirmed by using polyacrylamide gel electrophoresis (Figures S4 and S5). In addition, zeta potential analysis, electrochemical impedance spectroscopy, and CV were employed to monitor the stepwise electrode modification process (Figure S6). Reaction conditions, including material concentration, strand concentrations, and hybridization times, were optimized, and the data are summarized in Figures S7 and S8.

The performance of the proposed ECL biosensor in miR-155 detection was systematically investigated under the optimal conditions. As shown in Figure 5A, increasing miR-155 concentrations from 1 aM to 10 nM led to a gradual decrease in ECL intensity, reflecting a concentration-dependent quenching effect. The sensor response remained stable across all concentration levels (Figure 5B). A calibration curve was constructed by plotting ECL intensity (I_{ECL}) against the logarithm of miR-155 concentration (log c) in the range of 10 aM to 1 nM. The resulting linear regression equation was $I_{ECL} = -802.32 \log(c) - 311.59$, with a correlation coefficient (R^2) of 0.9952 (Figure 5C). The limit of detection (LOD), calculated at an S/N of 3, was 4.7 aM (Figure S9). This demonstrates that the sensor has outstanding sensitivity, outperforming many previously reported miR-155 detection platforms (Table S2). The stability of the biosensor was assessed through 10 consecutive ECL measurements using 10 fM miR-155 as the target. The relative standard deviation (RSD) was calculated to be 0.79% (Figure 5D), which is indicative of an excellent stability. What's more, the reproducibility of the designed biosensor was also tested (Figure S10).

To evaluate biosensor specificity, several nontarget microRNAs, including miR-21, miR-105, miR-93-3p, and miR-221, at a high concentration (100 nM) were used as potential interferents. As shown in Figure 5E, these miRNAs caused minimal changes in the ECL intensity. In contrast, the presence of 10 nM miR-155 alone caused a significant quenching effect. Moreover, miR-155 in the presence of interfering miRNAs produced ECL signals comparable to miR-155 alone, which confirms the sensor's high specificity for the target sequence.

Analysis of Human Serum Samples using the Proposed ECL Biosensor. To assess its practical applicability, the proposed biosensor was employed to detect miR-

155 in real biological samples using the standard addition method. Synthetic miR-155 with known concentrations was spiked into normal human serum, and the corresponding recovery rates were calculated. As summarized in Table S3, the recoveries ranged from 95.5% to 102.3%, demonstrating that the biosensor has high accuracy and can reliably detect the target in complex matrices. Furthermore, endogenous miR-155 expression was evaluated in human lung epithelial cells (BEAS-2B) and lung cancer cells (A549). Total RNA was extracted using the Trizol method, and varying cell counts were analyzed. As shown in Figure 5F, the ECL intensity exhibited a clear inverse relationship with the cell count. Additionally, a more pronounced decrease was observed in A549 cells compared to BEAS-2B cells at the same concentrations. This result confirms that miR-155 was significantly upregulated in lung cancer cells, consistent with previously reported studies.[45,46] Collectively, these findings validate the biosensor's potential for the quantitative analysis of miRNA biomarkers in clinical samples.

CONCLUSION

In summary, we developed a highly sensitive and selective ECL biosensor for miR-155 detection based on a self-enhanced Ln-MOF emitter. The antenna effect of H_3BTC effectively enhanced the ECL efficiency of Tb^{3+}, while the incorporation of Cu^{2+} and AgNPs into the Tb-BTC framework promoted coreactant catalysis and facilitated electron transfer, respectively. This synergistic configuration reduced the spatial distance between the luminophore and reactive intermediates, resulting in the amplification of the ECL emission. To enable signal modulation and target recycling, a Pd@Cu_2O-based quencher was introduced and combined with a dual-output TMSD amplification strategy. The resulting "on−off" ECL-RET platform had a wide detection range from 10 aM to 1 nM and an ultralow detection limit of 4.7 aM. The biosensor also had excellent selectivity and reproducibility and was successfully applied to analyze serum and cellular samples. This work proposes a generalizable strategy for designing multifunctional Ln-MOF-based ECL systems, presenting a promising platform for the ultrasensitive detection of microRNA biomarkers in clinical diagnostics.

ASSOCIATED CONTENT

Supporting Information

The Supporting Information is available free of charge at https://pubs.acs.org/doi/10.1021/acs.analchem.5c04977.

> Reagents, apparatus, sequence information for the DNA oligonucleotides; XPS spectral of other elements in CTBA, FTIR spectra of H3BTC, Tb-BTC, and CuTb-BTC; stability and reproducibility of CTBA, feasibility of dual-output (TMSD) amplification strategy; characterization of modified ECL biosensor; optimization of experimental conditions; detection limit; reproducibility of biosensor; supplementary figures; supplementary tables; and references (DOCX)

AUTHOR INFORMATION

Corresponding Authors

Pinyi Ma − *College of Chemistry, Jilin Province Research Center for Engineering and Technology of Spectral Analytical Instruments, Jilin University, Changchun 130012, China;* orcid.org/0000-0002-3230-4928; Email: mapinyi@jlu.edu.cn

Daqian Song − *College of Chemistry, Jilin Province Research Center for Engineering and Technology of Spectral Analytical Instruments, Jilin University, Changchun 130012, China;* orcid.org/0000-0002-4866-1292; Email: songdq@jlu.edu.cn

Authors

Ruiyan Liu − *College of Chemistry, Jilin Province Research Center for Engineering and Technology of Spectral Analytical Instruments, Jilin University, Changchun 130012, China*

Zhuoxin Ye − *College of Chemistry, Jilin Province Research Center for Engineering and Technology of Spectral Analytical Instruments, Jilin University, Changchun 130012, China*

Yongli Wu − *College of Chemistry, Jilin Province Research Center for Engineering and Technology of Spectral Analytical Instruments, Jilin University, Changchun 130012, China*

Yan Zhang − *College of Chemistry, Jilin Province Research Center for Engineering and Technology of Spectral Analytical Instruments, Jilin University, Changchun 130012, China*

Mo Ma − *College of Chemistry, Jilin Province Research Center for Engineering and Technology of Spectral Analytical Instruments, Jilin University, Changchun 130012, China; School of Pharmacy, Jilin University, Changchun 130012, China*

Complete contact information is available at: https://pubs.acs.org/10.1021/acs.analchem.5c04977

Notes

The authors declare no competing financial interest.

ACKNOWLEDGMENTS

This work was supported by the National Natural Science Foundation of China (22074052 and 22004046) and the Science and Technology Developing Foundation of Jilin Province of China (20240404044ZP).

REFERENCES

(1) Li, L.; Chen, Y.; Zhu, J.-J. *Anal. Chem.* **2017**, *89* (1), 358−371.

(2) Ye, Z.; Ma, M.; Chen, Y.; Yang, J.; Zhao, C.; Diao, Q.; Ma, P.; Song, D. *Anal. Chem.* **2024**, *96* (45), 17984−17992.

(3) Yao, L.; Zhi, J.; Wang, W.; Li, Q.; Jiang, D.; Chen, X.; Chen, Z. *Microchim. Acta* **2025**, *192* (3), No. 130.

(4) Wang, C.; Zhang, J.; Pei, Y.; Li, C.; Li, Y.; Chen, S.; Wang, Z. *Food Chem.* **2024**, *451*, No. 139461.

(5) Chen, L.; Wei, J.; Chi, Y.; Zhou, S. F. *ChemElectroChem* **2019**, *6* (15), 3878−3884.

(6) Shang, L.; Shi, B.-J.; Zhang, W.; Jia, L.-P.; Ma, R.-N.; Xue, Q.-W.; Wang, H.-S. *Anal. Chem.* **2022**, *94* (37), 12845−12851.

(7) Chen, Z.; Li, X.; Yang, C.; Cheng, K.; Tan, T.; Lv, Y.; Liu, Y. *Adv. Sci.* **2021**, *8* (20), No. 2101883.

(8) Li, Y.; Karimi, M.; Gong, Y.-N.; Dai, N.; Safarifard, V.; Jiang, H.-L. *Matter* **2021**, *4* (7), 2230−2265.

(9) Meng, Y.; Pu, J.; Gan, J.; Li, J. *Luminescence* **2022**, *37* (7), 1109−1119.

(10) Liu, J.-L.; Zhang, J.-Q.; Zhou, Y.; Xiao, D.-R.; Zhuo, Y.; Chai, Y.-Q.; Yuan, R. *Anal. Chem.* **2021**, *93* (31), 10890−10897.

(11) Pang, J. J.; Yao, Z. Q.; Zhang, K.; Li, Q. W.; Fu, Z. X.; Zheng, R.; Li, W.; Xu, J.; Bu, X. H. *Angew. Chem., Int. Ed.* **2023**, *62* (7), No. e202217456.

(12) Zhao, L.; Song, X.; Ren, X.; Wang, H.; Fan, D.; Wu, D.; Wei, Q. *Biosens. Bioelectron.* **2021**, *191*, No. 113409.

(13) Dong, H.; Liu, S.; Liu, Q.; Li, Y.; Xu, Z.; Li, Y.; Wei, Q. *Anal. Chem.* **2022**, *94* (37), 12852−12859.

(14) Chen, L.-L.; Kim, V. N. *Cell* **2024**, *187* (23), 6451−6485.

(15) Konno, M.; Koseki, J.; Asai, A.; Yamagata, A.; Shimamura, T.; Motooka, D.; Okuzaki, D.; Kawamoto, K.; Mizushima, T.; Eguchi, H.; et al. *Nat. Commun.* **2019**, *10* (1), No. 3888.

(16) Shao, C.; Yang, F.; Qin, Z.; Jing, X.; Shu, Y.; Shen, H. *BMC Cancer* **2019**, *19* (1), No. 1103.

(17) Anwar, S. L.; Aryandono, T.; Haryana, S. M. *Ann. Oncol.* **2019**, *30*, ix10−ix11.

(18) Habbe, N.; Koorstra, J.-B. M.; Mendell, J. T.; Offerhaus, G. J.; Ryu, J. K.; Feldmann, G.; Mullendore, M. E.; Goggins, M. G.; Hong, S.-M.; Maitra, A. *Cancer Biol. Ther.* **2009**, *8* (4), 340−346.

(19) Xiao, S.; Yang, Y.-T.; Chen, Y.-F.; Liu, J.-L.; Chai, Y.-Q.; Yuan, R. *Biosens. Bioelectron.* **2024**, *254*, No. 116193.

(20) Gao, T.-B.; Zhang, J.-J.; Wen, J.; Yang, X.-X.; Ma, H.-b.; Cao, D.-K.; Jiang, D. *Anal. Chem.* **2020**, *92* (1), 1268−1275.

(21) Ma, M.-N.; Zhuo, Y.; Yuan, R.; Chai, Y.-Q. *Anal. Chem.* **2015**, *87* (22), 11389−11397.

(22) Lei, Y.-M.; Zhou, J.; Chai, Y.-Q.; Zhuo, Y.; Yuan, R. *Anal. Chem.* **2018**, *90* (20), 12270−12277.

(23) Jiang, X.; Wang, H.; Chai, Y.; Shi, W.; Yuan, R. *Anal. Chem.* **2020**, *92* (13), 8992−9000.

(24) Gu, C.; Ji, S.; Chen, Z.; Yang, W.; Deng, Y.; Zhao, M.; Huang, W.; Yang, W.; Xu, W. *Biosens. Bioelectron.* **2025**, *279*, No. 117398.

(25) Li, Y.-X.; Li, J.; Cai, W.-R.; Xin, W.-L.; Marks, R. S.; Zeng, H.-B.; Cosnier, S.; Zhang, X.; Shan, D. *Anal. Chem.* **2020**, *92* (23), 15270−15274.

(26) Lian, X.; Yan, B. *RSC Adv.* **2016**, *6* (14), 11570−11576.

(27) Ge, K.; Chen, G.; Zhang, D.; Hao, J. N.; Li, Y. *Angew. Chem., Int. Ed.* **2024**, *63* (45), No. e202411956.

(28) Li, X.; Zhao, X.; Chu, D.; Zhu, X.; Xue, B.; Chen, H.; Zhou, Z.; Li, J. *Surf. Interfaces* **2022**, *33*, No. 102247.

(29) Kuo, C.-H.; Hua, T.-E.; Huang, M. H. *J. Am. Chem. Soc.* **2009**, *131* (49), 17871−17878.

(30) Luo, J.; Liang, D.; Zhao, D.; Yang, M. *Biosens. Bioelectron.* **2020**, *151*, No. 111976.

(31) Meng, D.; Zhao, T.; Busko, D.; Cosgun Ergene, A.; Richards, B. S.; Howard, I. A. *Adv. Opt. Mater.* **2024**, *12* (9), No. 2300867.

(32) Chen, Y.; Ye, Z.; Ma, M.; Yang, J.; Liu, R.; Zhang, Y.; Ma, P.; Song, D. *Biosens. Bioelectron.* **2024**, *254*, No. 116241.

(33) Chen, F.; Luo, L.; Liu, J.; Xing, Y.; Yang, X.; Xue, Y.; Ouyang, X. *ACS Sens.* **2024**, *9* (11), 5906−5914.

(34) Yu, J.; Sun, Y.; Geng, K.; Huang, J.; Cui, Y.; Hou, H. *Inorg. Chem.* **2024**, *63* (14), 6526−6536.

(35) Rej, S.; Wang, H.-J.; Huang, M.-X.; Hsu, S.-C.; Tan, C.-S.; Lin, F.-C.; Huang, J.-S.; Huang, M. H. *Nanoscale* **2015**, *7* (25), 11135−11141.

(36) Xue, J.; Yang, L.; Jia, Y.; Wang, H.; Zhang, N.; Ren, X.; Ma, H.; Wei, Q.; Ju, H. *ACS Sens.* **2019**, *4* (10), 2825−2831.

(37) Yang, X.; Lin, X.; Zhao, Y.; Zhao, Y. S.; Yan, D. *Angew. Chem., Int. Ed.* **2017**, *56* (27), 7853−7857.

(38) Steemers, F. J.; Verboom, W.; Reinhoudt, D. N.; van der Tol, E. B.; Verhoeven, J. W. *J. Am. Chem. Soc.* **1995**, *117* (37), 9408−9414.

(39) Tauc, J.; Grigorovici, R.; Vancu, A. *Phys. Status Solidi B* **1966**, *15* (2), 627−637.

(40) Peng, X.; He, Y.; Tan, K.; Yuan, R.; Chen, S. *Sens. Actuators, B* **2025**, *430*, No. 137343.

(41) Liu, T.-Y.; Qu, X.-L.; Yan, B. *Dalton Trans.* **2019**, *48* (48), 17945−17952.

(42) Quan, X.; Xu, X.; Yan, B. *J. Hazard. Mater.* **2022**, *427*, No. 127869.

(43) Wang, C.; Li, Z.; Ju, H. *Anal. Chem.* **2021**, *93* (44), 14878−14884.

(44) Al-Shehri, A. S.; Zaheer, Z.; Alsudairi, A. M.; Kosa, S. A. *ACS Omega* **2021**, *6* (41), 27510−27526.

(45) Zhou, P.; Pan, Y.; Pan, W.; Lu, S.; Yin, J.; Li, N.; Tang, B. *Anal. Chem.* **2022**, *95* (2), 1280−1286.

(46) Zhu, H.-Z.; An, J.-H.; Yao, Q.; Han, J.; Li, X.-T.; Jiang, F.-L.; Chen, G.-P.; Peng, L.-N.; Li, Y.-S.; Sun, J.-G.; Chen, Z. T. *Molecules* **2014**, *19* (9), 14710−14722.